



Aerothermal Aspects of a Pulsated Inclined Film Cooling Jet in Crossflow

Michel Mansour,* Vipluv Aga,⁺ Chokani Ndaona,[†] Reza S. Abhari[§]
Swiss Federal Institute of Technology Zurich, Zurich, Switzerland

The present work is conducted to extend the experimental database for validation of an enhanced 3D film cooling model. This paper reports the simultaneous measurements of the pressure and temperature field of streamwise film cooling jet over a flat plate with 30° flow angle. Turbine representative operating conditions and geometry are studied. The main flow is heated at a temperature above the injected coolant to simulate a density ratio of 1.29, while the blowing ratio is maintained at average value of 2. The measurements are performed using a novel fast-response entropy probe, which enables the simultaneous measurement of time-resolved total temperature and pressure. These two measurements are then combined to obtain the kinetic energy loss coefficient and the entropy change, as well as the streamwise baroclinic vorticity production term. The effect of unsteadiness on the aerothermal field, aerothermal losses and baroclinic vorticity is documented. Pulsation is seen to increase the aerothermal losses and baroclinic vorticity production compared to a steady jet.

Nomenclature

BR	=	blowing ratio
Cp_o	=	total pressure loss coefficient
D	=	injection hole diameter
DR	=	density ratio
f	=	pulsation frequency
f_r	=	reduced hole pulsation frequency
I	=	current
IR	=	momentum flux ratio
\dot{m}_c	=	coolant massflow
\dot{m}_f	=	freestream massflow
Ma	=	Mach number
p_o	=	total pressure
$p_{o,ref}$	=	reference total pressure
\dot{q}''_{cond}	=	conductive surface heatflux
\dot{q}''_{conv}	=	convective surface heatflux
R	=	ideal gas constant
Re	=	Reynolds number
S	=	pitch
t	=	time

*Research Assistant, Laboratory for Energy Conversion, Department of Mechanical and Process Engineering, michel.mansour@lec.mavt.ethz.ch (corresponding author), AIAA Member

⁺Research Assistant, Laboratory for Energy Conversion, Department of Mechanical and Process Engineering

[†]Senior Scientist, Laboratory for Energy Conversion, Department of Mechanical and Process Engineering, AIAA Associate Fellow

[§]Professor, Laboratory for Energy Conversion, Department of Mechanical and Process Engineering, AIAA Senior Member

T	=	time period
T_{f1}	=	thin film 1 temperature
T_{f2}	=	thin film 2 temperature
T_o	=	total temperature
$T_{o,ref}$	=	reference total temperature
U_c	=	coolant absolute velocity
U_f	=	freestream absolute velocity
V	=	voltage
X	=	axial coordinate
Y	=	lateral coordinate
Z	=	vertical coordinate
α	=	injection angle
ζ	=	entropy loss coefficient
θ	=	nondimensional temperature
μ	=	dynamic fluid viscosity
ν	=	kinematic fluid viscosity
ξ	=	kinetic energy loss coefficient
ρ	=	fluid density

I. Introduction

The main interests in the improvement of film cooling for turbines are an increase of efficiency and the enhancement of the lifetime of blades. The latter results directly in a significant reduction of engine cost and is therefore a key issue for the aeroengine industry. Previous film-cooling studies have primarily concentrated on measurements of surface heat transfer and adiabatic effectiveness, using methods such as thin film gages [1], thermocouples and thermochromic liquid crystals [2, 3] and infrared camera [4].

Although, film cooling has primarily focused on heat transfer issues, engine designers are also concerned with aerothermodynamic losses that results from film cooling injection. The aerodynamic mixing effect due to film cooling injection has been studied by previous researchers [5-8]. However it should be noted that most of these studies were performed at conditions in which the coolant and freestream temperatures are equal, due to the inability to simultaneously measure pressure and temperature, especially in the practically relevant situation involving unsteady flows. Thus the effect of unsteady thermal gradients on aerothermodynamic losses has not been characterized in previous studies.

The present work is conducted within the framework of a broader computational and experimental program at ETH Zurich. The computational component of this program is focused on the development of a feature-based film cooling model. This film cooling model obviates the need to use highly resolved meshes near film cooling holes. Thus with 3D Reynolds-averaged Navier-Stokes (RANS) solvers, solutions can be obtained with two orders of magnitude faster computations. The film cooling model is embedded in a RANS code using an implicit immersed boundary method. The model is described in detail in Burdet [9], Burdet and Abhari [10, 11] and Burdet et al. [12]. The model accounts for the macroflow features of the injected jet including trajectory, penetration, secondary flows and mixing. The parameters of the model are anchored to a large set of 3D PIV measurements that have been made in the film cooling facility at ETH Zurich. The PIV measurements have included the flow structure of both streamwise, Bernsdorf, et al. [13] and compound angled, Aga et al. [14] film cooling holes. The present work is thus, in part, conducted to extend this experimental database for validation of an enhanced film cooling model. The results presented here include detailed measurements of the time-resolved and time-averaged temperature, pressure, and entropy. These measurements are made possible due to the recent development at ETH Zurich of a fast response entropy probe. The effect of the baroclinic vorticity and the effect of jet pulsation, which is representative of the periodic unsteadiness within a turbine, is also examined. The measurements are performed on a hole with streamwise injection

II. Experimental methodology

A. Experimental set up

A schematic of the test section and measurement arrangement is shown in Figure 1. The test section consists of a

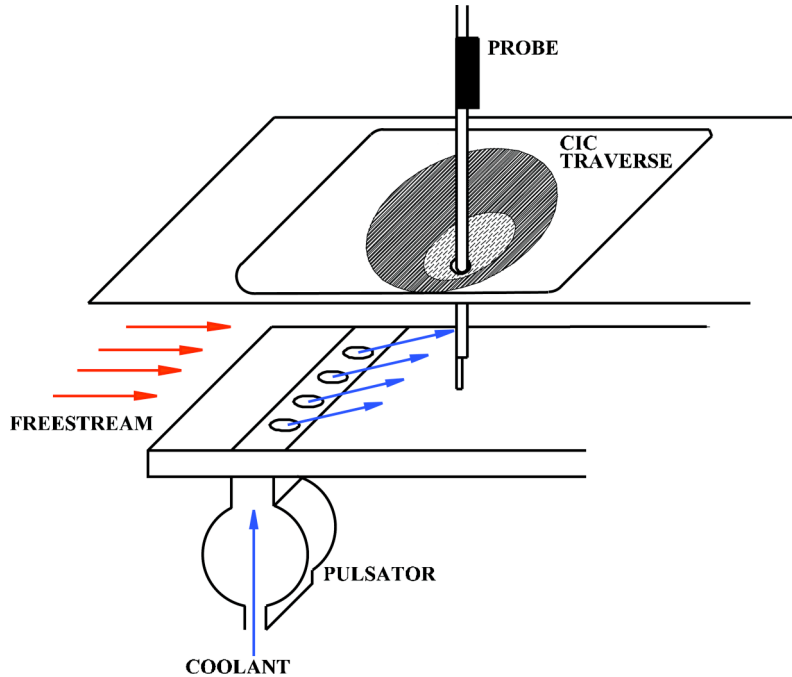


Figure 1: Schematic of LAVAL test section

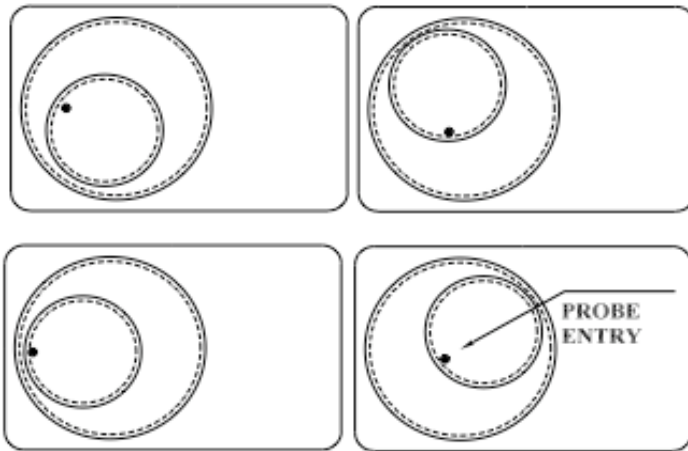


Figure 2: Schematic of the Circle in Circle (CIC) plane traversing system for probe access shown in different configurations allowing flexible spatial access.

During operation of the test rig the flow parameters are adjusted with the aid of the real-time monitoring system. Forty primary data channels (pressure, temperature, frequency and mass flow) are acquired directly from their corresponding sensors. The most relevant parameters like main flow Mach number, blowing ratio and density ratio are displayed online, thus allowing their fast and accurate adjustment. The test rig is described in more detail in Bernsdorf [15].

rectangular flow path of dimensions 40×181 mm in cross-section. The freestream flow, which can be heated up to 120°C , is powered by a centrifugal compressor. The boundary layer thickness is controlled by a suction arrangement comprised of 327 discrete holes of 1.2 mm diameter stacked over an area of 60×180 mm; this area is immediately upstream of the location of the film cooling injection holes. The cooling flow is delivered, through interchangeable MACOR inserts, by a shop air system with a maximum 75 g/s mass flow rate. This dried air can be cooled to -60°C . As Figure 1 shows, the coolant air enters through a pulsator, which delivers steady air when switched off and pulsed coolant air at frequencies up to 500 Hz when switched on. Various pressure and temperature probes at different points allow a real time monitoring and measurement of the conditions within the rig.

Probe measurements were accomplished using a novel probe traversing and access technique, henceforth referred to as the Circle-In-Circle (CIC) system. This traversing system is made of two circular metal plates fitted onto a flat plate. The two non-concentric circular disks can each rotate about their own axes and thereby allow the probe entry hole, to be located at any point in the plane, as shown in Figure 2. The probe itself can be traversed perpendicular to the plane of the traversing system as shown in Figure 1 thereby allowing access to any measurement point within the 3D domain. The sealing between the moving circles is accomplished by use of tight clamps. The main advantage of this probe traverse system over the other approaches is the ease of manufacture, flexibility in spatial access and ability to move the probe without any other force than that from the four axis traversing system that moves the probe assembly itself.

As seen in Figure 3 the diameter of the injection hole is $D = 7\text{mm}$. The hole pitch is $S = 4D$, and the hole has a surface angle $\alpha = 30^\circ$. The flow field was measured at three planes, $X/D = 3, 4, 6$, that are normal to the primary freestream velocity. The centre of the hole is at the origin of the coordinate system. In each crossplane the measurement grid is comprised of 15 equally spaced points in the vertical direction, and 19 points, in the lateral direction, that are clustered close to the centre of the injection holes.

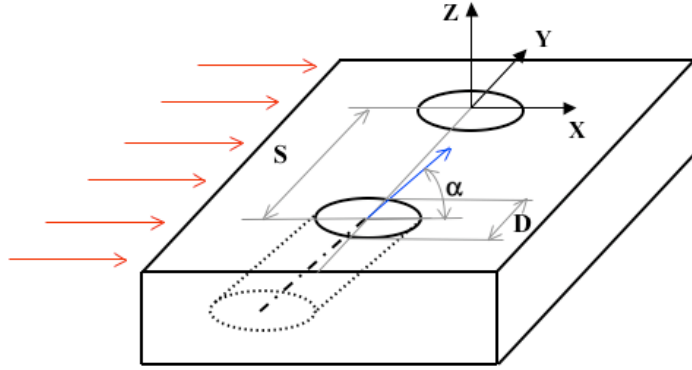


Figure 3: Definition of the coordinate system and geometrical parameters

B. Operating Conditions

The local Reynolds number Re_D , based on the hole diameter and the coolant flow properties is defined by Eq. 1.

$$Re_D = \frac{\rho_c U_c D}{\mu_c} \quad \text{Eq. 1}$$

It is assumed that for $Re_D > 5000$ the coolant flow is fully turbulent, see Schlichting and Gersten [16]. As film-cooled blades are generally designed for the first stages of high-pressure turbines, they are immediately downstream of the combustor chamber. The present measurements are performed at a freestream Mach number of $Ma = 0.3$, which corresponds to a freestream velocity of $U_f = 120\text{ m/s}$ and thus to a Reynolds number $Re_D = 46000$.

The rotor-stator interactions in a turbine affect the coolant jets in a way which can be mimicked as a pulsating jet, such effects have been shown in Abhari and Epstein [1]. The strength of the jet blowing is very dependent on the near-hole flow conditions. Therefore a measure of the near-hole jet unsteadiness is introduced, Eq. 2, through the reduced frequency.

$$f_r = \frac{fD}{U_f} \quad \text{Eq. 2}$$

The pulsating frequency f is often triggered by the wake passing frequency of the rotor stage. In general the near-hole reduced frequency f_r is much less than 1. Thus in addition to a steady injection case, an unsteady injection case with a pulsation frequency of $f = 400\text{Hz}$, which corresponds to a reduced frequency of $f_r = fD/U_f = 0.025$, is examined. The reduced frequency of $f_r = 0.025$ is representative of a real gas turbine engine condition (Burdet [9]).

The density ratio DR , Eq. 3, is used to quantify the thermal difference between the hot freestream and the coolant fluid.

$$DR = \frac{\rho_c}{\rho_f} \quad \text{Eq. 3}$$

In the present measurements, a density ratio of 1.3 is obtained by maintaining the coolant at room temperature (300 K) and the heated freestream at 393 K. Due to the limitations in the measurement and calibration of the probe these ranges could not be extended to match full-scale gas turbine engine operating conditions, where typical density ratios are in the range of $DR = 1.8$. The massflux and momentum of the coolant jet relative to the freestream are quantified by the blowing ratio BR and momentum flux ratio IR , see Eq. 4 and Eq. 5.

$$BR = \frac{\rho_c U_c}{\rho_f U_f} \quad \text{Eq. 4}$$

$$IR = \frac{BR^2}{DR} \quad \text{Eq. 5}$$

In general, the mean blowing ratio on the pressure and suction sides of a film-cooled blade varies between 0.5 and 3.0. A blowing ratio of 0.5 corresponds to a coolant jet that tends to remain attached to the wall, whereas a blowing ratio of 3.0 indicates that the coolant jet is detached from the wall and penetrates through the freestream boundary layer, see for instance Leylek and Zerkel [17]. The measurements were conducted at a mean blowing ratio of $\overline{BR} =$

2, which leads to a momentum flux ratio of $IR = 3.07$. Table 1 summarizes the main parameters of the test rig and measurement configuration.

Mach number (freestream), Ma	0.3	Reynolds number, number $Re_d = U_f D / \nu$	46000
Injection surface angle, α [°]	30	Density ratio, $DR = \rho_c / \rho_f$	1.3
Hole diameter, D [mm]	7	Mean blowing ratio, $\overline{BR} = \rho_c U_c / \rho_f U_f$	2
Freestream temperature, T_f [K]	393	Momentum flux ratio, $IR = BR^2 / DR$	3.07
Coolant Temperature, T_c [K]	303	Reduced frequency, $f_r = f D / U_f$	0 & 0.025

Table 1: Main parameters of test condition in the film cooling facility

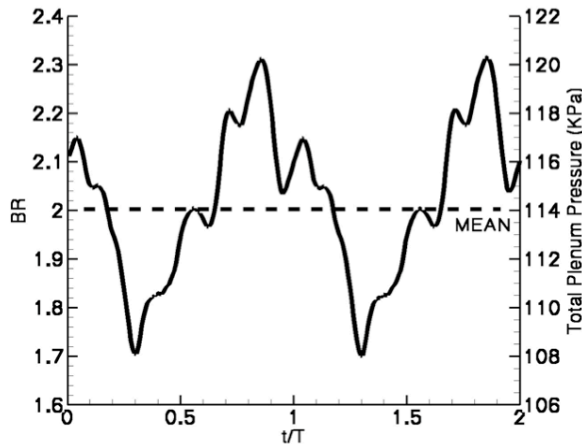


Figure 4: Temporal variations of the blowing ratio and plenum pressure for $BR=2$, $DR=1.3$ and $f_r=0.025$.

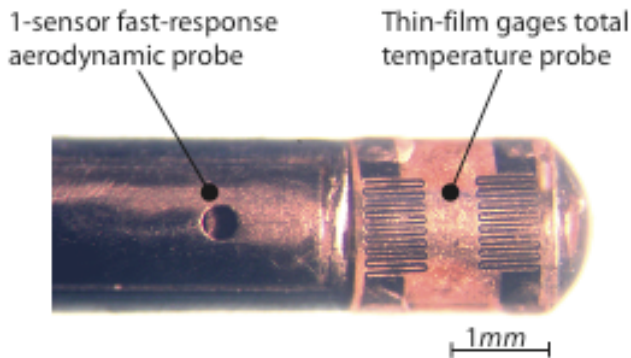


Figure 5: Photograph of the tip of the unsteady entropy probe.

The variations of the total pressure in the plenum of the injection holes and the corresponding local blowing ratio BR are shown in Figure 4 for the unsteady injection case. The duty cycle is a little above 50% and the BR variation is a little above 0.3 as can be seen in Figure 4.

C. Measurement Technology

The flowfield measurement device is a fast-response entropy probe (FENT), Figure 5, which has been recently developed at ETH Zurich. The principal components of the FENT probe are a fast response aerodynamic probe (FRAP) and an unsteady total temperature probe. The diameter of the cylindrical probe is 1.8mm. The design, manufacture and calibration of FRAP is well established at ETH Zurich and detailed in Grossweiler et al. [18], Kupferschmied et al. [19], Pfau et al. [20] and Schlienger [21]. The FRAP is comprised of a miniature silicon piezoresistive chip, working on the principal of the Wheatstone bridge, which is glued beneath a pressure tap to measure the unsteady total pressure. The basic element of the unsteady total temperature probe is a pair of thin-film gages that are deposited onto a semi-cylindrical fused quartz substrate. The thin-film gages are made of 200nm-thick nickel and are operated as resistance thermometers. The serpentine shaped sensor is 30 μ m wide and covers a rectangular area of 0.55mm \times 0.85mm. When the thin-film gages are electrically heated to two different

temperatures, T_{f1} and T_{f2} , the convective heat transfer can be expressed as follows:

$$\begin{aligned}\dot{q}_{conv1}'' &= \alpha(T_o - T_{f1}) \\ \dot{q}_{conv2}'' &= \alpha(T_o - T_{f2})\end{aligned}\quad \text{Eq. 6}$$

The total temperature of the flow, T_o can therefore be determined from:

$$T_o = T_{f1} + \frac{\dot{q}_{conv1}''(T_{f2} - T_{f1})}{\dot{q}_{conv1}'' - \dot{q}_{conv2}''}\quad \text{Eq. 7}$$

The Joulean heating of the thin-film gages is balanced by the conductive and convective heat losses. Thus the convective heat transfer for each gage is given by:

$$\dot{q}_{conv}'' = VI - \dot{q}_{cond}''\quad \text{Eq. 8}$$

The thin-film gages are operated in a constant current mode, and thus the first term on the right-hand side of Eq. 8 is readily determined. On the other hand, the second term on the right-hand-side of Eq. 8 is estimated using an unsteady, semi-infinite, heat conduction model. The bandwidth of the conduction model used in the present work is 400Hz to 120kHz with a phase shift of less than 5°. However the FRAP that is integral to the FENT probe limits the bandwidth of the FENT probe to 48 kHz.

Pressure and temperature signals are acquired simultaneously at a frequency of 100 kHz over a period of 2 seconds. The offset between the thin-film gages and the pressure sensor is 2.25mm. During the data processing coincident phase-locked measurements of 250 samples of p_0 and T_0 are used to determine the unsteady relative entropy. Therefore when phase-locked averaged data are considered, the spatial resolution of the measurements is given by the area covered by the thin film gages, which is 0.85mm × 1.77mm.

D. Uncertainty Analysis

The errors in the freestream pressure and temperature are in the range of 0.1 to 0.3 percent relative to the quantities being measured. The details of the uncertainty calculation for these inlet conditions are given by Bernsdorf [13]. Considering the time-resolved entropy probe, several sources contribute to the total temperature derived from the unsteady total temperature sensor. The propagation error technique is used to combine the uncertainties in these sources into a composite value. The derivation of the unsteady total temperature is based on Eq. 7. Therefore the uncertainty in the unsteady total temperature measurements depends on the uncertainties associated with to the measurements of the thin film total temperatures, (T_{f1} , T_{f2}), and the convective heat transfer rates, \dot{q}_{conv1}'' , \dot{q}_{conv2}'' . The relative errors in the convective heat transfer and the measured thin film temperatures are $\Delta\dot{q}_{conv}'' / \dot{q}_{conv}'' = \pm 3.77\%$ and $\Delta T_{f1, f2} / T_{f1, f2} = 1\%$, respectively. These yield a relative error of 2.5% in the total temperature. The uncertainty in the time resolved total pressure is $\pm 100Pa$, Pfau et al [22]. Table 2 summarizes the relative measurement errors in the derived flow quantities.

Parameter	Relative uncertainty [%]
Ma	0.52
DR	0.26
BR	2.6
IR	5.00
f_r	0.54
Entropy change, Δs	2.7

Table 2: Error estimates of derived quantities

III. Results and Discussion

A. Aerothermal Losses

The simultaneous pressure and temperature measurements are used to infer quantities such as total pressure loss coefficient and entropy generation. Estimates of loss in turbomachinery applications are best described by the change of entropy generation. However, a difficulty arises in defining a proper reference temperature and reference pressure that are used to calculate the change in entropy production for the jet in crossflow situation. Ascribing loss to the reference conditions of the freestream conditions, neglects the losses arising from the cooling hole. A logical way to take into account this two temperature and pressure problem is to use a reference condition which is a mass weighted average of the two initial conditions of the hot freestream and the coolant in the plenum. This approach was used by Wilfert and Fottner [5] to reference the pressure losses from a film cooling hole in a turbine. $P_{o,ref}$ and $T_{o,ref}$ are defined by Eq. 9 and Eq. 10, respectively. It is evident that this approach assumes that the fluid that is measured downstream has arrived from a single initial condition given by $P_{o,ref}$ and $T_{o,ref}$.

$$P_{o,ref} = \frac{\dot{m}_c}{\dot{m}_f + \dot{m}_c} P_{o,c} + \frac{\dot{m}_f}{\dot{m}_f + \dot{m}_c} P_{o,f} \quad \text{Eq. 9}$$

$$T_{o,ref} = \frac{\dot{m}_c}{\dot{m}_f + \dot{m}_c} T_{o,c} + \frac{\dot{m}_f}{\dot{m}_f + \dot{m}_c} T_{o,f} \quad \text{Eq. 10}$$

These reference conditions are used to define a total pressure loss coefficient, Cp_o , defined by Eq. 11, where U_f is the inlet freestream velocity.

$$Cp_o = \frac{P_{o,ref} - P_o}{\frac{1}{2} \rho U_f^2} \quad \text{Eq. 11}$$

The aerothermal performance of film cooling jets is most often characterised by a film cooling loss coefficient. This is the ratio of the kinetic energy at a point downstream of injection, after mixing has occurred, to the sum of the kinetic energy that the freestream and coolant flows would have had, were they to isentropically arrive at the measurement point. This definition is explained in detail in [5, 23]. The loss coefficient, ξ is defined in Eq. 12. The advantage of using this definition is that the losses in both the freestream and the coolant holes are considered. Additionally, an ideal reference condition, as described in Eq. 9 and Eq. 10 does not need be estimated.

$$\xi = 1 - \frac{\left(1 + \frac{\dot{m}_c}{\dot{m}_f}\right) T_o \left(1 - \frac{P_s}{P_o}\right)}{T_{o,f} \left(1 - \frac{P_s}{P_{o,f}}\right)^{\frac{\gamma-1}{\gamma}} + \frac{\dot{m}_c}{\dot{m}_h} T_{o,c} \left(1 - \frac{P_s}{P_{o,c}}\right)^{\frac{\gamma-1}{\gamma}}} \quad \text{Eq. 12}$$

Unlike the calculation of ξ in other works such as [5, 23], Eq. 12 includes an engine representative temperature gradient. Previous measurements of the loss coefficient, ξ have primarily been estimated with pressure probes in DR = 1 conditions. However, as is shown later, the temperature gradients have a significant effect on the thermal mixing loss generation.

Since the commonly used pressure loss and kinetic loss coefficients do not take into account all the aerothermal losses of the flow, the entropy creation term is a better indicator of mixing and separation losses. The entropy creation Δs is given by:

$$s - s_{ref} = c_p \ln \left(\frac{T_o}{T_{o,ref}} \right) - R \ln \left(\frac{P_o}{P_{o,ref}} \right) \quad \text{Eq. 13}$$

The entropy creation term is non-dimensionalised and plotted in the subsequent figures as an entropy function $e^{-\Delta s/R}$. Thus, an area where $e^{-\Delta s/R}$ is low signifies an area of great loss as the entropy change from the reference condition is higher. As defined in Denton [24] an entropy loss coefficient, Eq. 14, is also defined at every measurement point using the local temperature and velocity. This coefficient is primarily used for comparing the mass-weighted averaged value for different flow conditions in the subsequent sections.

$$\zeta = \frac{T \Delta s}{0.5 \cdot U^2} \quad \text{Eq. 14}$$

The total pressure loss coefficient, C_{p_o} , as defined in Eq. 11, is plotted in Figure 6 for a crossplane at a streamwise location of $X/D = 6$ with and without pulsation of the film cooling. The wake shows up as a region of highest total pressure loss and the windward side of the jet as intermediate value of pressure loss. The pulsated case, $f_r = 0.025$, shows a larger spread in Z/D direction of total pressure loss coefficient. It can be argued that the C_{p_o} detects regions of pure aerodynamic loss even though other losses are taking place.

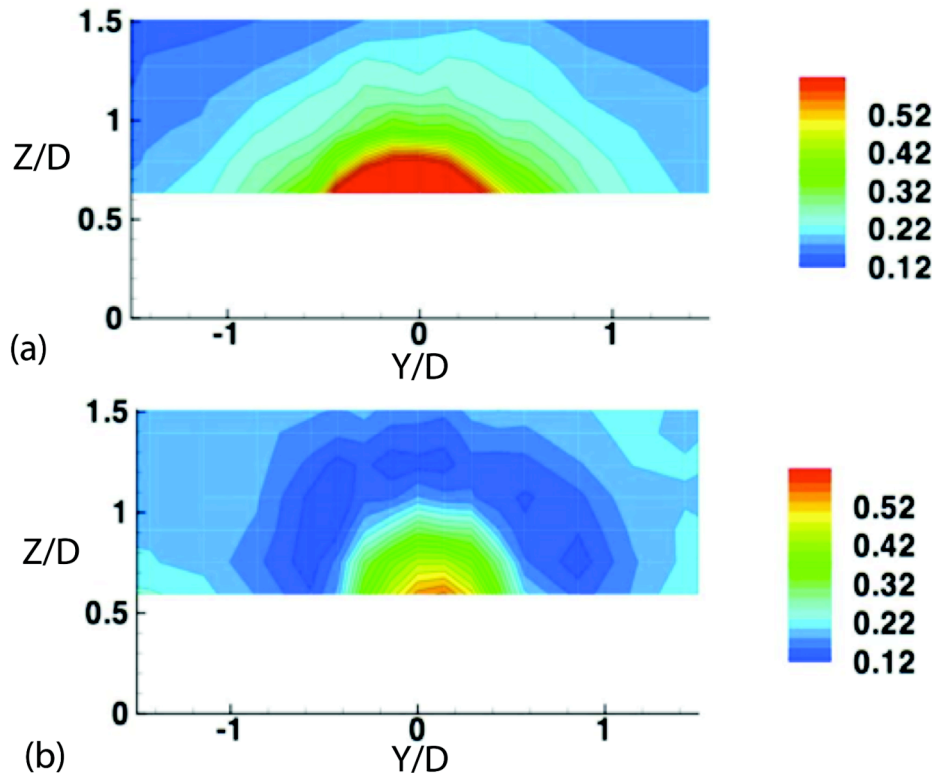


Figure 6: Time averaged contours of total pressure coefficient, C_{p_o} at $X/D = 6$, for (a) $f_r = 0$ Hz and (b) $f_r = 0.025$

Figure 7 shows the time averaged entropy function change with respect to the reference conditions as described in Eq. 9 and Eq. 10 and the local total temperature within a film cooling jet. The local total temperature T_o is non-dimensionalised using Eq. 15:

$$\theta = \frac{T_o - T_{o,h}}{T_{o,c} - T_{o,h}} \quad \text{Eq. 15}$$

where $T_{o,h}$ and $T_{o,c}$ are the freestream and coolant inlet total temperatures, respectively. It is clear that due to time-averaging the temperature distributions (a) and (b) are almost identical for the steady and pulsating film cooling cases, except for part of the flow in below $Z/D = 0.5$ which could not be measured due to probe access constraints

for the steady film cooling case. However, at high pulsation frequency it has been shown in Bernsdorf et al. [13] that the pulsating flow is quasi-steady such that it has almost the same flow-structure as a non-pulsating flow when viewed from a time-averaged perspective. This is not the case for the entropy function distribution which shows higher levels entropy creation for the pulsated case, especially in the region around $Z/D = 0.5$. The time-averaged plots, thus give only partial insight into the actual comparison because as seen in Figure 4, the BR variation over a pulsation period is almost 0.6, which leads to a smearing of the temperature and pressure distribution in the wake.

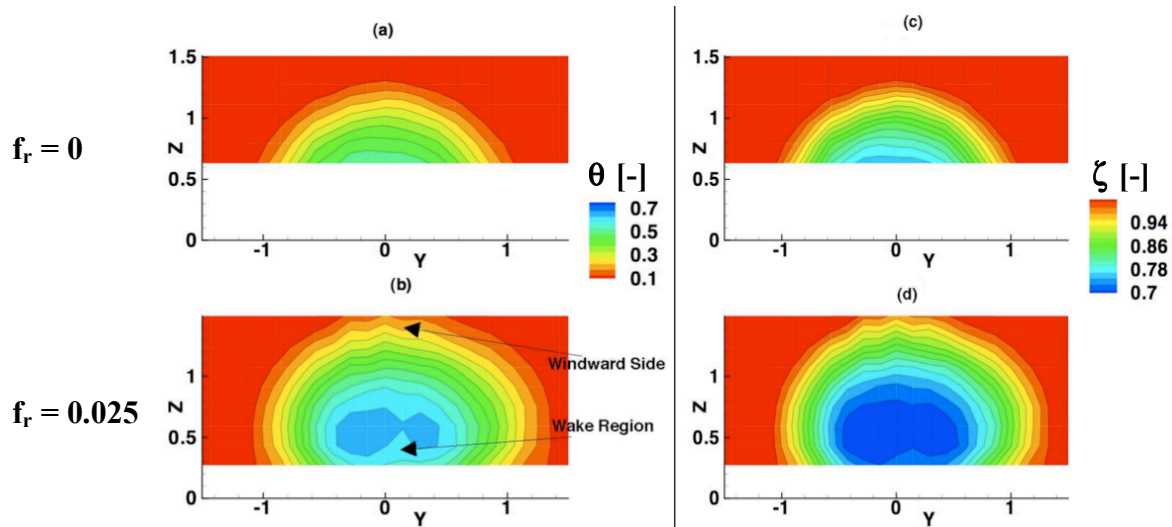


Figure 7: Time averaged contours of non-dimensionalized temperature (left column) and entropy function (right column), at $X/D = 6$ for $f_r = 0$ (top row) and $f_r = 0.025$ (bottom row)

Figure 8 and Figure 9 show the non-dimensionalized temperature contours in a space-time diagram for the unsteady injection case. In Figure 8 a single pulsation period is plotted at two time instants and the non-dimensionalized temperature, θ , distributions are shown at three X/D locations from left to right. Figure 9 shows the corresponding non-dimensionalized temperature, θ , distributions along the streamwise direction at $Y/D = 0$ at the two time instants. Both measurements provide a qualitative description of the jet behavior during a pulsation. Phase lock averaging is done with respect to the optical trigger of the pulsator, see Bernsdorf [15]. The temperature distribution of the coolant downstream of the hole doesn't disappear completely with the pulsation of the jet, but becomes smaller and travels closer to the wall, as the effect of the trough in massflow passes through. The high frequency of the pulsation is partially responsible for this effect as the time scale at which the thermal energy dissipates is much higher than the time scale at which the massflow oscillates. The gradients in temperature are most evident at $X/D = 3$, and maintain their relative levels even during a pulsation. The temperature gradients mix out further downstream as seen in at $X/D = 6$, Figure 8. This shows that temperature mixing is primarily driven by the counter rotating vortex pair (CVP) and the jet penetration near the hole downstream region ($X/D < 5$). In Figure 9 the expansion of the thermal field and its evolution away from the wall during the crest of the pulsation wave is observed along the streamwise direction at $Y/D = 0$. The jet lifting reduces strongly the thermal protection [25-27]. Previous simulations presented by Burdet and Abhari [11], performed at $BR = 1.25$ and $DR = 1.3$ confirm the time-resolved observations of a high blowing ratio ($BR \geq 1.25$) oscillating jet.

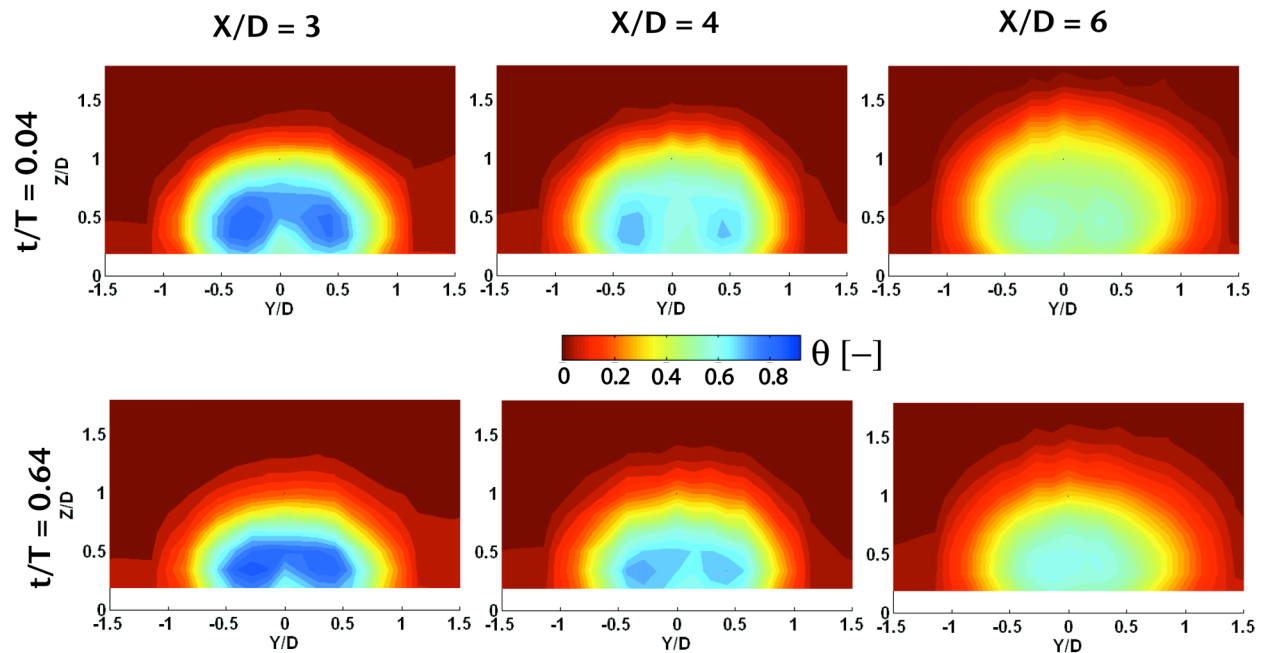


Figure 8: Space time diagram for $BR = 2$, $DR = 1.3$, unsteady film cooling jet showing contours of non-dimensionalized temperature, θ , at $X/D = 3, 4, 6$ and at different pulsation time instants within a pulsation

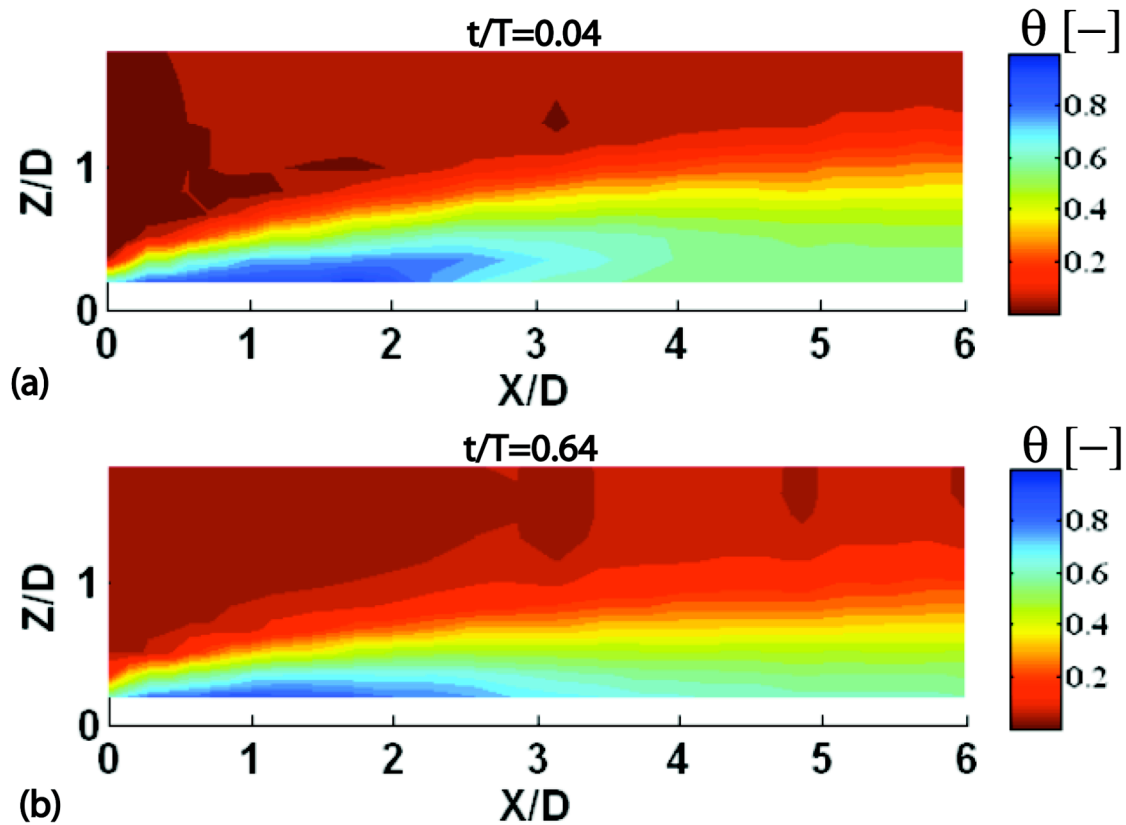


Figure 9: Space time diagram for $BR = 2$, $DR = 1.3$, unsteady film cooling jet showing contours of non-dimensionalized temperature, θ , along streamwise direction at $Y/D = 0$ and at different pulsation time instants within a pulsation

Similar to Figure 8, Figure 10 shows the entropy function distribution in a space-time diagram for $f_r = 0.025$. The entropy change takes into account the change in both temperature and pressure. The similarity of the temperature and entropy distributions suggests that the temperature gradients dominate over the pressure gradients the entropy generation. The locations of high entropy generation occur within the coolant core, which get their characteristic kidney vortex shape from the separation in the coolant hole. Comparing the jet at $X/D = 3$ for the time instants $t/T = 0.4$ and $t/T = 0.64$, it can be concluded that the jet becomes smaller when the entropy change is maximum is within the coolant core, which is where the lowest temperature is found. At $X/D = 6$ the lateral extent of the jet becomes larger due to entrainment because the CVP causes greater mixing out of the coolant with the hot stream. This mixing out translates into a more uniform distribution of entropy change. These results suggest that, for high density ratios, entropy change is strongly dependent on the temperature distribution.

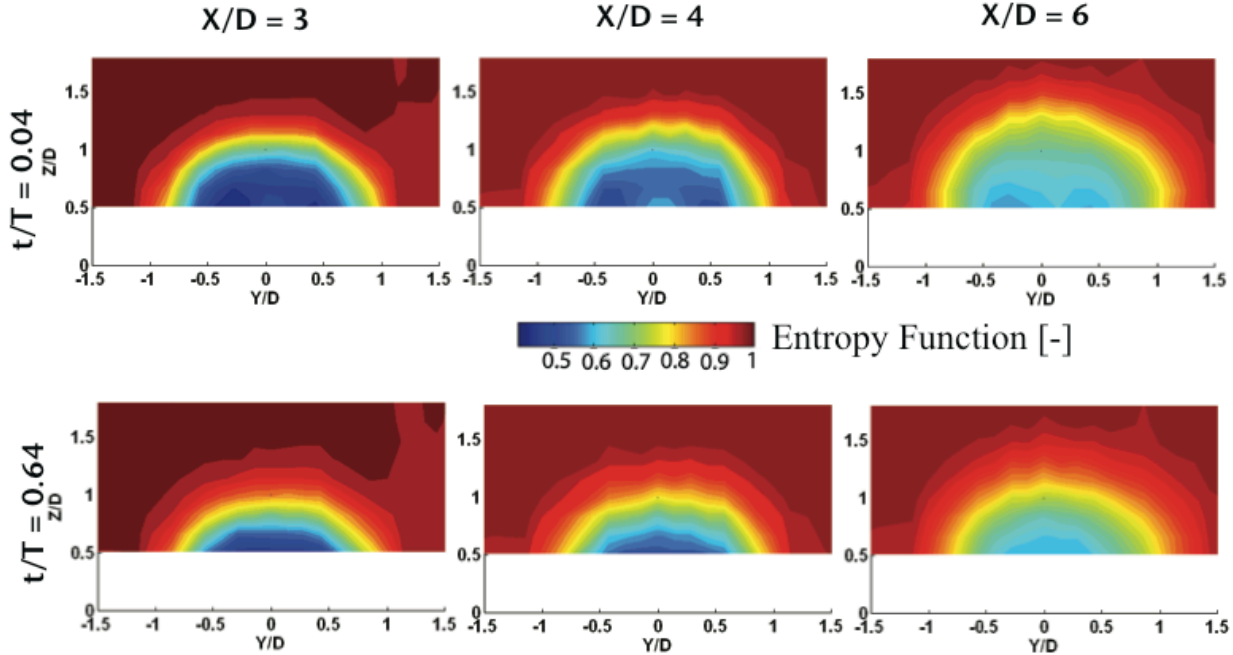


Figure 10: Space time diagram for $BR = 2$, $DR = 1.3$, unsteady film cooling jet showing contours of entropy function at $X/D = 3, 4, 6$ and at different pulsation time instants within a pulsation

In order to get averaged quantities of performance which can be conveniently interpreted, the total pressure loss coefficient, C_{p_0} , kinetic energy loss coefficient, ξ , and entropy loss coefficient, ζ are mass flow averaged at the measurement planes using Eq. 16, where F represents the quantity being averaged.

$$F = \frac{\iint F \rho V dA}{\iint \rho V dA} \quad \text{Eq. 16}$$

1. Total Pressure Loss Coefficient

Figure 11 shows the mass averaged total pressure coefficient for different conditions. It is conjectured that this quantity indicates the total pressure loss from the cooling hole as well as that suffered by the main flow during the mixing process. In general, the loss coefficient increases for downstream stations as mixing progresses. Pulsating jets tend to have higher pressure losses on an average than steady jets. This is because, total pressure losses are caused due to non-isentropic momentum mixing as well as separation within the coolant metering length, which are enhanced by pulsation.

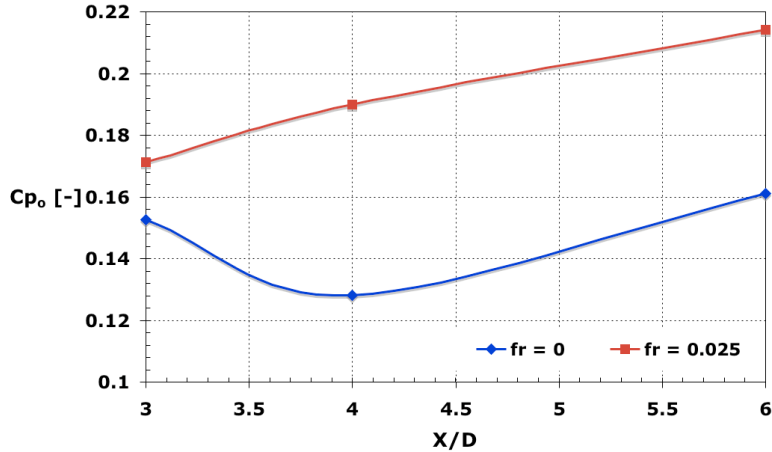


Figure 11: Evolution of mass flow weighted average of total pressure loss coefficient, C_{p_o} , at $X/D = 0.3$ and $X/D = 0.6$ with and without pulsation ($f_r = 0$ & 0.025)

Figure 12 shows the change in the mass-weighted pressure loss coefficient for measurement planes at $X/D = 3$ and 6 at different phases within a pulsation cycle. The change in loss coefficient during a pulsation increases with downstream distance as well as there is about 40% change in the loss coefficient during a pulsation cycle. The maxima and minima of the pressure loss coefficient do not correspond to the crest and trough of the coolant jet as defined by the jet size at that particular station. As the pressure fluctuations understandably have a different time scale from the temperature field fluctuations such a consequence is to be expected.

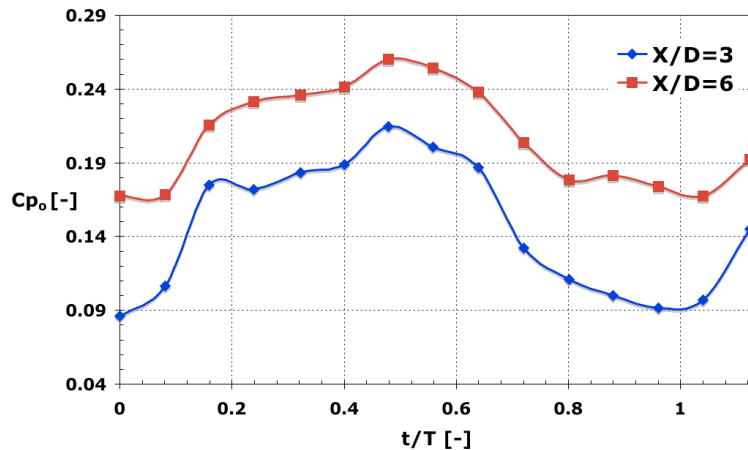


Figure 12: Evolution of time-resolved mass flow weighted average total pressure, C_{p_o} , of a pulsating jet at $X/D = 3, 6$

2. Kinetic Energy Loss Coefficient

The kinetic energy loss coefficient as described in Eq. 6 has been often used to describe the performance of film cooling geometries by taking into account losses in jet and freestream both. This loss coefficient indicates both the mixing loss and separation losses in kinetic energy suffered by the jet and freestream in a combined manner. Figure 13 indicates that the trends are similar to the pressure loss curve, i.e. overall the pulsated injection shows higher losses than the steady one and grows with downstream distance. A difference between Figure 13 and Figure 11 can be noted in terms of the relative difference of loss increase with pulsation. The KE loss also has contribution from the thermal field, which though changing less aggressively still makes a contribution to loss. This extra effect is enhanced by the pulsation and hence shows up as a greater difference.

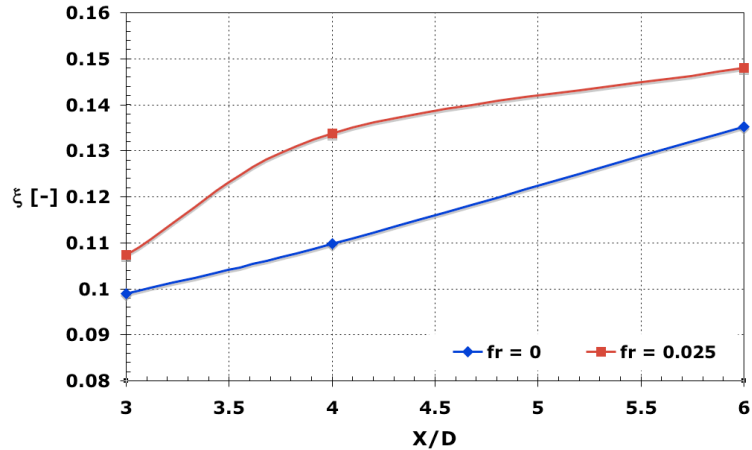


Figure 13: Evolution of mass flow weighted average of kinetic energy loss coefficient, ξ , at $X/D = 0.3$ and $X/D = 0.6$ with and without pulsation ($f_r = 0$ & 0.025)

Figure 14 shows the time resolved KE loss coefficient. Both the curves are qualitatively very similar to the C_{pt} loss plot of Figure 12. The crest and trough of the jet is not correlated with the maxima and minima of the KE Loss coefficient. It appears that the kinetic energy loss coefficient variation lags the variation of the low temperature jet regions by about half a cycle. The size of the coolant core does not seem to affect the variation of the KE loss too much as it mimics mainly the pressure losses. It is suspected therefore that the contribution of thermal mixing to the loss is underestimated by this definition.

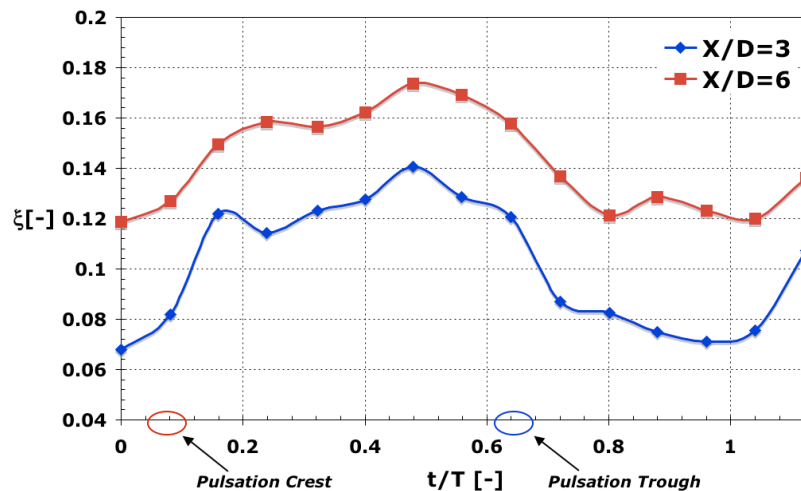


Figure 14: Evolution of time-resolved mass flow weighted average kinetic energy loss coefficient, ξ , of a pulsating jet at $X/D = 3, 6$

3. Entropy Loss Coefficient

Entropy change has been advocated as the most physically relevant loss parameter by Denton [25] for turbomachinery analysis. The entropy loss coefficient primarily shows the losses the freestream suffers due to (a) viscous dissipation (b) mixing of mass, momentum and energy and (c) heat transfer. Due to the modified definition of the reference quantities described by Eq. 10 and 11, this loss coefficient would also indicate the losses that the jet itself suffers within the hole and during ejection. Figure 15 shows the time averaged entropy loss coefficient evolution with downstream distance for pulsated and non-pulsated cases. On an average the pulsated case is about 75% times larger for all downstream locations compared to the non-pulsated case. Compare this to the 40% loss enhancement indicated by the pressure loss coefficient as per Figure 11. A second feature is the relative growth of the entropy loss coefficient with downstream distance. The previous two definitions showed a sizeable growth of the loss with downstream distance, however the entropy loss coefficient exhibits a smaller growth in loss. This can be

explained by the fact that entropy loss is dominated by the temperature mixing, whereas the KE loss and pressure loss coefficients are dominated by the momentum mixing. A streamwise jet does show high momentum transfer due to the mixing effect of the counter-rotating vortex pair (CVP), but this same CVP, confines the coolant jet within the wake thereby preventing high thermal mixing. Pulsating a jet causes high changes in not only the momentum mixing but also the penetration into the freestream changes periodically. The alternate separation and reattachment of the jet causes a very high momentum but also thermal mixing. This effect is captured by the entropy loss definition.

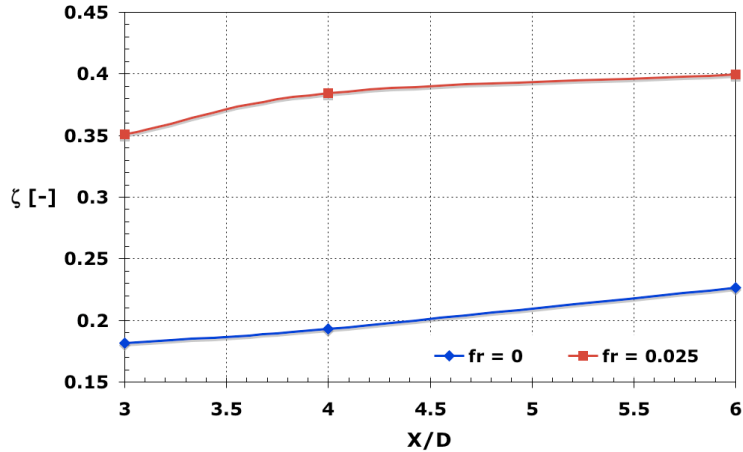


Figure 15: Evolution of mass flow weighted average of entropy loss coefficient, ζ , at $X/D = 0.3$ and $X/D = 0.6$ with and without pulsation ($f_r = 0$ & 0.025)

Figure 16 shows the entropy loss evolution for the pulsated jet at two different stations. The variation in entropy over a pulsation period is almost 70% of the average loss from crest to trough. It is however important to note that unlike similar graphs of Figure 12 and Figure 14, the trends shown in this figure are quite different. The entropy loss coefficient shows a maximum during the jet crest, that is when the coolant jet appears largest in the temperature visualizations of Figure 8.

The other definitions were not correlated with the size of the coolant jet but rather the incoming pressure field maxima. This shows the dominance of the thermal gradient and thermal mixing contribution to loss production. The differences in the time scales with which a change in velocity propagates compared to the convective transport of temperature by the jet body are responsible for these offsets especially since the pulsation frequency is very high. The mean level of loss as shown in Figure 16 increases with downstream distance from $X/D = 3$ to $X/D = 6$ but the relative level of variation remains the same.

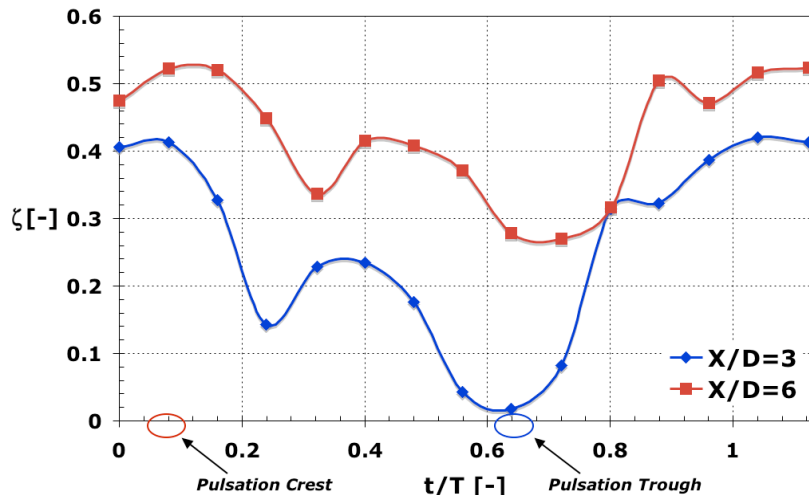


Figure 16: Evolution of time-resolved mass flow weighted average entropy loss coefficient, ζ , of a pulsating jet at $X/D = 3, 6$

B. Streamwise Baroclinic Vorticity Production

The vorticity is defined as:

$$\vec{\omega} = \nabla \times \vec{v} \quad \text{Eq. 17}$$

Eq. 18 shows the incompressible unsteady vorticity transport equation. The second term on the right hand side of Eq. 18, the baroclinic vorticity production term, Eq. 19, have not been considered in previous work like, [7, 8, 28, 29] due to a lack of accurate unsteady temperature measurement. However the FENT probe used in the present work allows this term to be determined

$$\frac{D}{Dt} \vec{\omega} = \vec{\omega} \cdot \nabla \vec{v} + \frac{1}{\rho^2} \nabla \rho \times \nabla p + \nabla \times F_{\text{viscous}} \quad \text{Eq. 18}$$

$$\omega_b = \frac{1}{\rho^2} \nabla \rho \times \nabla p \quad \text{Eq. 19}$$

Figure 17 shows the time averaged non-dimensionalized streamwise baroclinic vorticity production, as defined in Eq. 20, plotted at the measurement planes $X/D = 3, 4$ and 6 . In the following results the baroclinic vorticity is non-dimensionalized by the hole diameter D and the freestream velocity U_f , Eq. 20.

$$\hat{\omega}_b = \frac{\omega}{U_f D} \quad \text{Eq. 20}$$

The streamwise baroclinic vorticity production term is due to the interaction of the density gradient with the pressure gradient within the measurement plane. The highest levels of baroclinic vorticity are produced at $Z/D = 0.7$, which is within the vortex cores of the jet. This is due to the presence of high temperature and pressure gradients in the CVP. The produced vorticity at that location positively enhances the vorticity that is already present in CVP, thus adding vorticity to it and increasing the mixing of the jet. In the shear layer zone, the primary locations of baroclinic vorticity production correspond to areas where the pressure and density gradients are largely orthogonal. Compared to the unsteady PIV measurements performed at similar conditions by Bernsdorf et al [13] the contribution of the baroclinic vorticity term to the total vorticity is in the range of 10%. It should also be noted that as the jet is propagating downstream of the injection hole the pressure and temperature gradients tend to become smaller, thus at $X/D = 6$ the baroclinic vorticity production is reduced by 50% compared to the upstream position $X/D = 3$.

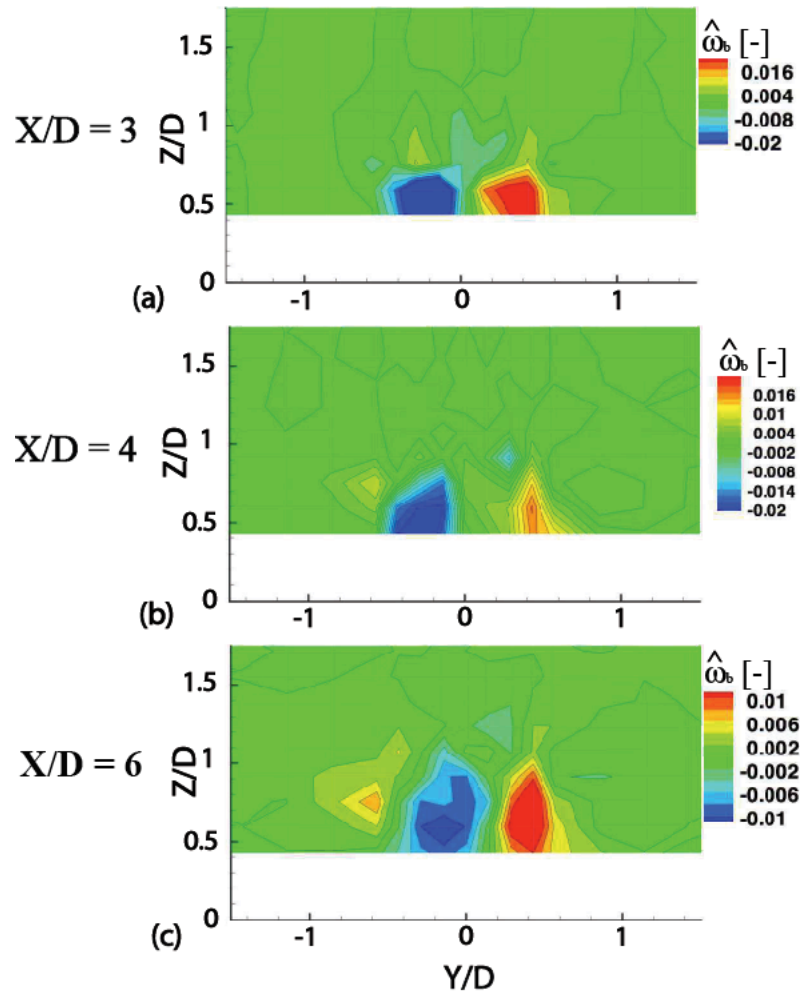


Figure 17: Time-averaged non-dimensionalized Baroclinic vorticity production at (a) $X/D = 3$ (b) $X/D = 4$ and (c) $X/D = 6$, for $DR = 1.3$ and $f_r = 0.025$

4. Density Effect on Baroclinic Vorticity Production

It has been noted in the previous section that the baroclinic vorticity production has significant impact on the total vorticity that is present in the jet. The impact of the density ratio on the baroclinic vorticity production term is now briefly discussed. The measurement at $X/D = 3$ for $DR = 1.04$, $BR = 2$, $f_r = 0.025$ is compared to the measurement for the case $DR = 1.3$, $BR = 2$, $f_r = 0.025$, Figure 18. The two baroclinic vorticity productions exhibit very similar distributions. However the reduced levels of density gradient present in the thermal field of the $DR = 1.04$ case causes a 75% reduction in baroclinic vorticity production in the core of the CVP compared to the $DR = 1.3$ case. It can be anticipated that the baroclinic vorticity production will be much more pronounced in a full-scale gas turbine engine, where typical density ratios are in the range of $DR = 1.8$.

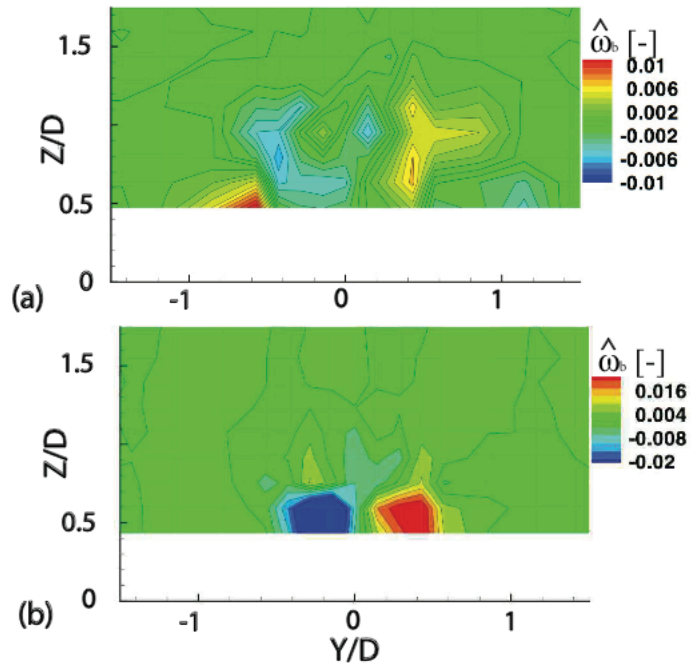


Figure 18: Baroclinic vorticity production at $X/D = 3$ for (a) $DR = 1.04$ and (b) $DR = 1.29$

5. Baroclinic Vorticity Production in a Pulsated Jet

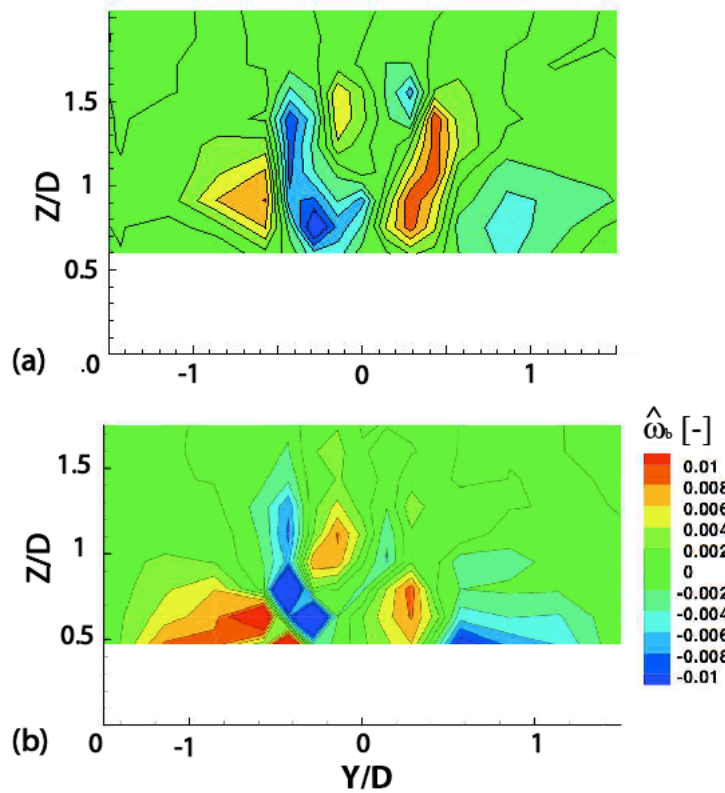


Figure 19: Time-averaged contours of baroclinic vorticity production, $X/D=6$ for $DR = 1.3$ (a) $f_r = 0.025$ and (b) $f_r = 0$

The effect of jet pulsation on the baroclinic vorticity production is now investigated. Figure 19 shows the time averaged contour of baroclinic vorticity for a pulsed ($f_r = 0.025$) and steady jet at $X/D = 6$ and for a density ratio of $DR = 1.3$. The two cases show similar distributions and amplitudes in baroclinic vorticity production. This result shows that the pulsation of the jet is not a parameter that influences the baroclinic vorticity production in the time-averaged frame.

However it is insightful to view the change in baroclinic vorticity for the pulsating jet. The relative variation in the baroclinic vorticity production over a cycle is shown in Figure 20, its fluctuation relates to the duty cycle of the pulsation, which is a little above ± 0.3 ($1.7 < \overline{BR} < 2.3$). Because of this, the trough of the baroclinic vorticity corresponds to around $t/T = 0.64$ at which time the jet is observed to have the smallest blowing ratio and shows highest baroclinic vorticity when the jet is at its largest blowing ratio ($t/T = 0.04$). In the time resolved frame the baroclinic vorticity in the jet are twice as high than in the time averaged frame.

Figure 20 provides insight into the vorticity production for a pulsating jet. During a crest the total circulation of the streamwise vorticity would be higher than that during the trough. This additional quantity would be underpredicted in typical film-cooling injection models that are used in CFD; because these models presently employ a constant circulation vortex

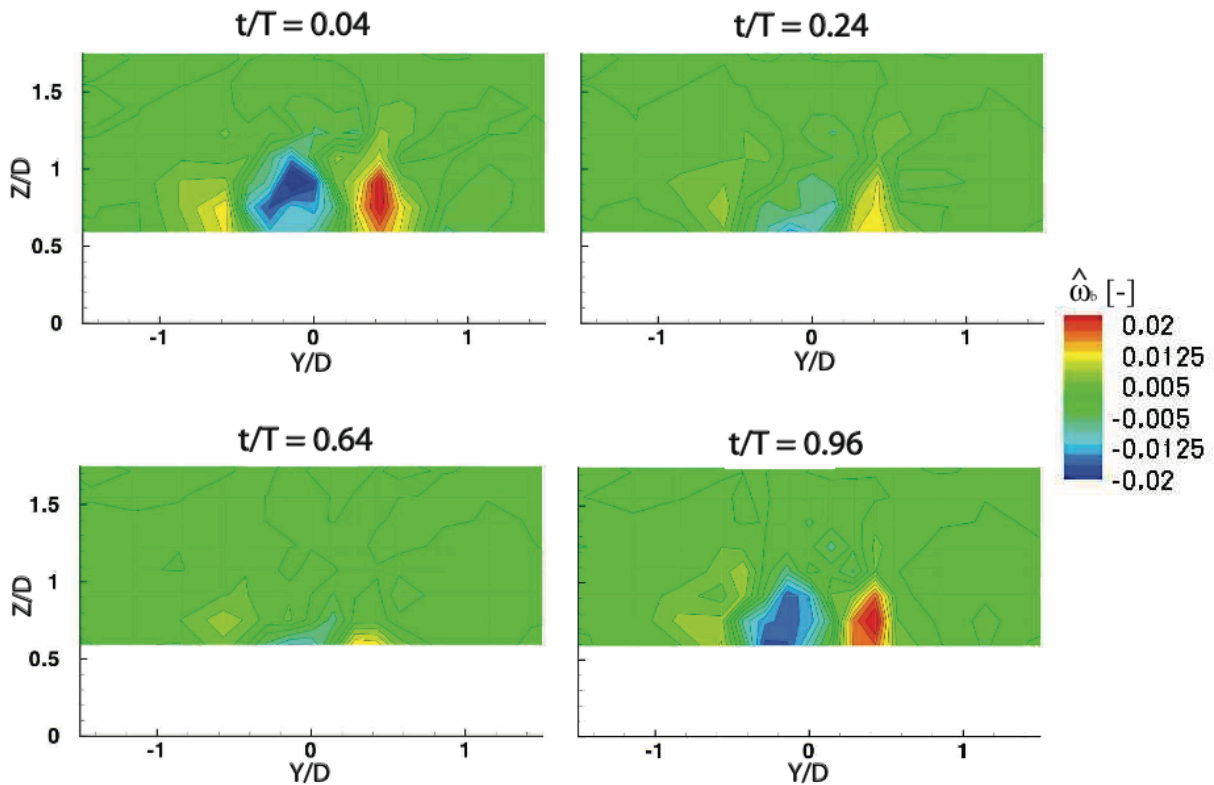


Figure 20: Baroclinic vorticity production over a pulsation period at $X/D = 6$ for the unsteady injection case, (a) $t/T = 0.08$; (b) $t/T = 0.24$; (c) $t/T = 0.64$ and (d) $t/T = 0.96$

III. Conclusion

A streamwise film cooling jet with 30° inclination angle was studied, with and without engine representative pulsation of hole diameter based reduced frequency of $f_r = 0.025$. A single operating point, viz. $BR = 2$, $DR = 1.3$, and $IR = 3.04$, was investigated in detail. Time resolved temperature, pressure and entropy data at different downstream planes served as the focal point for understanding the basic behaviour of the streamwise injection during pulsation. Mass-weighted inlet total pressures and temperatures were used as reference conditions to simultaneously determine the entropy change within the incoming jet and the freestream.

The averaged and time resolved entropy changes were seen to have high correlation with the local temperature distribution. It was observed that the wake of the streamwise jet has areas of high entropy generation. The cores of

the counter rotating vortex pair are the regions of highest entropy generation. As the jet mixes downstream the coolant spread increases and the areas of entropy production spread over a larger region; this spread is also seen in the temperature. One important observation during pulsation is that the position of the jet above the surface increases and decreases, thus reducing the thermal protection, as the jet tends to separate from the surface at the injection hole exit.

It has been shown that the entropy loss coefficient incorporates the loss due to momentum mixing, thermal mixing and separation losses near the hole exit. Whereas the total pressure loss coefficient, C_{p_0} , detects regions of pure aerodynamic loss, and the routinely used kinetic energy loss coefficient, ξ , reflects the losses due to separation and momentum mixing, but underpredicts the loss in thermal energy due to mixing.

The pulsating jet shows marked increase (75%) in aerothermal losses due to greater thermal mixing and enhanced shear layer losses due to the greater penetration and effective blowing ratio variation near the injection hole.

The fast response entropy probe provides a new insight in to the vorticity production term for a pulsating jet. It has been shown that the contribution of the streamwise baroclinic vorticity term relative to the total vorticity is in the range of 10%, and that in the time resolved frame, the baroclinic vorticity in the jet is twice as high than in the time-averaged frame. This additional quantity would be underpredicted in typical film-cooling injection models that are used in CFD. Moreover, it has been shown that the reduced levels of density gradient present in the thermal field of the $DR = 1.04$ case causes a 75% reduction in baroclinic vorticity production in the core of the counter rotating vortex pair compared to the $DR = 1.3$ case. It can be anticipated that the baroclinic vorticity production term will be much more pronounced in full-scale gas turbine engines, where typical density ratios of $DR=1.8$ are observed.

Acknowledgments

The authors gratefully acknowledge useful discussions with Dr. Martin Rose concerning the circle-in-circle traversing system. The authors also thank Cornel Reshef for his work in developing the electronic instrumentation and data acquisition system for the fast-response entropy probe.

References

- [1] R. S. Abhari and A. H. Epstein "An Experimental Study of Film Cooling in a Rotating Transonic Turbine," *ASME Journal of Turbomachinery*, vol. 11, pp. 818-827, 1994.
- [2] H. Reiss and A. Boeles, "Experimental Study of Shower Headcooling on a Cylindrical Shaped Holes," *ASME Journal of Turbomachinery*, vol. 122, pp. 161-169, 2000.
- [3] T. Furukawa and P. M. Ligrani, "Transonic Film Cooling Effectiveness from Shaped Holes on a Simulated Turbine Airfoil," *Journal of Thermophysics and Heat Transfer* vol. 16, pp. 228-237, 2002.
- [4] J. Dittmar, A. Schultz, and S. Wittig, "Assesment of Various Film Cooling Configurations Including Shaped and Compound Angle Holes Based on Large Scale Experiments," *ASME Journal of Turbomachinery*, vol. 125, pp. 57-64, 2003.
- [5] G. Wilfert and L. Fottner, "The Aerodynamic Mixing Effect of Discrete Film Cooling Jets with Mainstream Flow on a Highly Loaded Turbine Blade," *ASME Journal of Turbomachinery*, vol. 119, pp. 310-319, 1996.
- [6] S. Friedrichs, H. P. Hodson, and W. N. Dawes, "Aerodynamic Aspect of Endwall Film Cooling," *ASME Journal of Turbomachinery*, vol. 119, pp. 786-793, 1997.
- [7] R. Fearn and R. P. Weston, "Vorticity Associated with a Jet in Crossflow," *AIAA Journal*, vol. 1, pp. 1666-1671, 1974.
- [8] A. Eroglu and R. E. Breidenthal, "Structure, Penetration, and Mixing of Pulsated Jets in Crossflow," *AIAA Journal*, vol. 39, pp. 417-423, 2001.
- [9] A. Burdet, "A Computationally Efficient Feature-Based Jet Model for Prediction of Film-Cooling Flows," Diss. ETH No 16163, 2005.
- [10] A. Burdet and R. S. Abhari, "Three-Dimensional Flow Prediction and Improvement of a Film-Cooled Turbine Blade Using a Featured-Based Jet Model " *ASME Journal of Turbomachinery*, vol. 129, p. 258, 2007.
- [11] A. Burdet and R. S. Abhari, "Influence of Near Hole Pressure Fluctuation on the Thermal Protection of a Film-Cooled Flat Plate," ASME paper No. HT2007-321812, to appear in ASME Journal of Heat Transfer, 2008, 2007.
- [12] A. Burdet, R. S. Abhari, and M. Rose, "Modelling of Film Cooling - Part II: Model for Use in Three-Dimensional Computational Fluid Dynamics," *ASME Journal of Turbomachinery*, vol. 129, p. 221, 2007.
- [13] S. Bernsdorf, M. Rose, and R. S. Abhari, "Modeling of film cooling-part 1: Experimental study of flow structure," *ASME Journal of Turbomachinery*, vol. 128, pp. 141-149, 2006.
- [14] V. Aga, M. Rose, and R. S. Abhari, "Experimental Flow Structure Investigation of Compound Angled Film Cooling," *ASME Journal of Turbomachinery*, vol. 130, p. 031005, 2008.
- [15] S. Bernsdorf, "Experimental Investigation of Film Cooling Flow Structure," in *Diss. ETH, VDI, 7, Nr.476*, 2005.
- [16] H. Schlichting and K. Gersten, *Boundary Layer Theory*, 8th Revised and Enlarged Edition ed.: Springer-Verlag Berlin Heidelberg New-York, 2000.

- [17] J. H. Leylek and R. D. Zerckel, "Discrete-Jet Film Cooling: A Comparison of Computational Results with Experiments," *ASME Journal of Turbomachinery*, vol. 116, pp. 358-368, 1994.
- [18] C. Gossweiler, H. J. Humm, and P. Kupefrschmied, "The Use of Piezo-Resistive Semi-Conductor Pressure Transducers for Fast-Response Probe Measurements in Turbomachinery," in *Proc. 10th Symposium on Measuring Techniques for Transonic and Supersonic Flows in Cascades and Turbomachines*, Brussel, 1989.
- [19] P. Kuperfshried, P. Köppel, C. Roduner, and G. Gyarmathy, "On the Development and Application of The FRAP (Fast-Response Aerodynamic Probe) System for Turbomachines - Part 1: the Measurement System," *ASME Journal of Turbomachinery*, vol. 122, pp. 517-522, 2000.
- [20] A. Pfau, J. Schlienger, A. I. Kalfas, and R. S. Abhari, "Unsteady 3-Dimensional Flow Measurement Using a Miniature Virtual 4 Sensor Fast Response Aerodynamic Probe (FRAP)," in *ASME Paper No. GT-2003-38128* 2003.
- [21] J. P. Schlienger, "Evolution of Unsteady Secondary Flows in a Multistage Shrouded Axial Turbine," Diss. ETH, Nr. 15230, 2003.
- [22] A. Pfau, "Loss Mechanisms in Labyrinth Seals of Shrouded Axial Turbine," in *Diss. ETH, Nr. 15226*, 2003.
- [23] U. Drost, "An Experimental Investigation of Gas Turbine Airfoil Aero-Thermal Film Cooling Performance," in *PhD thesis, EPF Lausanne, Switzerland*, 1998.
- [24] J. D. Denton, "Loss Mechanisms in Turbomachines " *ASME Journal of Turbomachinney*, vol. 115, pp. 521-652, 1993.
- [25] C. Saumweber, A. Schultz, and A. Wittig, "Free-Stream Turbulence Effects on Film Cooling With Shaped Holes," *ASME Journal of Turbomachinery*, vol. 125, pp. 65-73, 2003.
- [26] S. Coulthard, R. J. Volino, and K. A. Flack, "Effect of Jet Pulsing on Film Cooling - Part I: Heat Transfer Results," *ASME Journal of Turbomachinery*, vol. 129, pp. 247-257, 2007.
- [27] S. Coulthard, R. J. Volino, and K. A. Flack, "Effect of Jet Pulsing on Film Cooling - Part II: Effectiveness and Flow-field Temperature Resultts," *ASME Journal of Turbomachinery*, vol. 129, pp. 232-246, 2007.
- [28] D. G. Bogard and K. A. Thole, "Gas Turbine Film Cooling," *AIAA Journal of Propulsion and Power*, vol. 22, pp. 249-270, 2006.
- [29] J. P. Bons, R. MacArthur, C. Pestian, and J. David, "The effect of unsteadiness on film cooling effectiveness," in *AIAA Paper No 1995-306*, 1995.